PCCP

Accepted Manuscript

ROYAL SOCIETY OF CHEMISTRY

www.rsc.org/pccp

Atomistic Bond Relaxation, Energy Entrapment, and Electron Polarization for the Rb_N and Cs_N Clusters ($N \leq 58$)

Yongling Guo,[a] Maolin Bo,[a] Yan Wang,[b] Yonghui Liu,[a] Yongli Huang,[a*] Chang Q Sun[c*]

[a]*Key Laboratory of Low-Dimensional Materials and Application Technologies (Ministry of Education), Hunan Provincial Key Laboratory of Thin Film Materials and Devices, Faculty of Materials Science and Engineering, Xiangtan University, Hunan 411105, China*

[b]*School of Information and Electronic Engineering, Hunan University of Science and Technology, Hunan 411201, China*

[c]*NOVITAS, School of Electrical and Electronic Engineering, Nanyang Technological University, Singapore 639798, Singapore*

*Email: huangyongli@xtu.edu.cn; ecqsun@ntu.edu.sg

Abstract

We systematically examined the effect of atomic undercoordination on the performance of bonds and electrons of Rb and Cs atomic clusters and their solid skins using a combination of photoelectron spectrometric analysis and density functional theory calculations. Results show that atomic coordination number reduction shortens the bonds by up to 30% for the Rb_{13} and Cs_{13} clusters, which densifies the local electrons and entraps their binding energies. Consistency between predictions and observations revealed that the Rb 4*p* level shifts from 13.654 eV for an isolated atom to the bulk value of 14.940 eV and the Cs 5*p* level shifts from 10.284 to 11.830 eV upon bulk formation. Such core-electron densification and entrapment polarize the valence charge from the inner to the outermost layer of skins, which perturbs the local Hamiltonian and hence dictates the unusual behavior of the Rb and Cs solid skins and nanocrystals.

Keywords: Rb and Cs solid skins, nanocrystals, bond strain, electron polarization, energy entrapment

1. Introduction

According to Pauling[1], the interatomic chemical bonds bridge the structure and properties of crystals and molecules. Therefore, one can mediate the performance of a substance by controlling the dynamics of bond relaxation and the associated energetics of electrons by localization, densification, entrapment, polarization, and transportation by various means such as atomic undercoordination[2]. Materials exhibit fascinating chemical and physical properties at undercoordinated atomic sites in the solid skins and nanocrystals[3-5], but generally, one often separates the solid skins from atomic clusters though they share the same attribute of atomic undercoordination. Nanocluster formation not only tunes the known bulk properties such as elastic modulus and melting temperatures but also creates properties that the parent bulk never demonstrates[6, 7]. For example, conductor-insulator transition[8] occurs at the nanometer scales or clusters containing ~100 atoms. A gold crystal of a few nanometer size is an excellent catalysts though its bulk counterpart is chemically inert[9, 10]. The catalytic ability is even stronger for atom at the even less coordinated edges and apexes.

Due to the unique attribute of Rb and Cs, they have important applications in many high-tech areas such as electronic devices[11], catalysts[12], specialty glass[13], biochemistry[14], etc. Besides, Rb and Cs exhibit strong vitality in transformation of thermionic generator, ion propulsion engine, laser, electric power device, and ion cloud communication[15-17]. Therefore, Rb and Cs solid skins and clusters have attracted much attention with focus on the electronic structures of skins or crystals at the nanometer scale[18, 19].

However, the mechanism of the electronic structure change at the skin or cluster remains an issue of debating. Cluster size reduction induced conductor-insulator transition[8] is attributed to quantum confinement[20, 21] and the skin induced energy shift is attributed to the "initial-final state" relaxation mechanism[22]. Therefore, a systematic study reconciling the solid skins and atomic clusters is desirably meaningful[5, 23, 24].

In this communication, we show that interaction between undercoordinated atoms of the chemically active Rb and Cs, perturbs the local Hamiltonian that dictates the electronic behavior of these two elements universally. In addition, we also correlate core level binding energy (BE) to the cluster size and shape with the aid of density functional theory (DFT) calculations and X-ray photoelectron spectroscopy (XPS) measurements. Results confirmed our predictions that atomic undercoordination shortens and stiffens bonds in the skins and

atomic clusters, which dictates the unusual behavior of solid skins and atomic clusters.

2. Principles and methods

2.1 Bond order-length-strength (BOLS) notion

The BOLS notion[9, 25, 26] states that if an atomic bond breaks, the remaining ones become shorter and stronger[2]. Consequently, local bond strain and electron entrapment take place immediately nearby the broken bonds. The local strain and quantum entrapment densely localizes the charge and energy, which modifies the elemental quantities, such as atomic cohesive energy[4, 27], electro-affinity[28], Hamiltonian[29], work function[30], and Young's modulus[31]. Such electronic densification and entrapment may further rationalize the strong localization premise of Philip Anderson[32] to the undercoordinated systems.

The BOLS premise suggests that a bond between undercoordinated atoms[33] contracts from the bulk value of d_b to $d_z = C_z d_b$ and the bond energy increases from the bulk standard of E_b to $E_z = C_z^{-m} E_b$. The C_z is the bond contraction coefficient $C_z = d_i / d_b = 2/\{1+\exp[(12-z_i) /(8z_i)]\}$, which varies only with the effective atomic coordination number (CN) and has nothing to do with the dimensionality or the structure phase. The m is the bond nature index, and for metals[34], $m = 1$.

According to the tight-binding (TB) theory[35], the integral of the intra-atomic potential $V_{atom}(r)$ and the Bloch wave-function determine the vth energy level of an isolated atom, $E_v(0)$. The involvement of the inter-atomic potential $V_{crys}(r)$ shifts deeper the core level $\Delta E_v(z)$. The single-body Hamiltonian describes the total energy of a specific electron:

$$\hat{H} = \left[-\frac{\hbar^2 \nabla^2}{2m} + V_{atom}(r) \right] + V_{crys}(r)(1 + \Delta_H) \tag{1}$$

The atomic energy level and its z-dependent shift in the vth level follow the relationships[9]:

$$E_v(0) = \langle v,i|V_{\text{atom}}(r)|v,i\rangle$$
$$\Delta E_v(z) = E_v(z) - E_v(0)$$
$$= \langle v,i|V_{\text{crys}}(r)|v,i\rangle + \sum_{j=1}^{j=z}\langle v,j|V_{\text{crys}}(r)|v,j\rangle = \alpha\left(1+\frac{z\beta}{\alpha}\right) \cong \alpha \propto E_z \quad (2)$$

The energy shift $\Delta E_v(z)$ is proportional to the cohesive energy E_z of a bond between the z-coordinated atoms. The $|v,i\rangle$ is the eigen wave-function at the ith atomic site with z neighbors. The α is the exchange integral and the β is the overlap integral. The term $z\beta/\alpha << 1$ because of $\langle v,i|v,j\rangle = \delta_{ij}$, with the Kronig function δ_{ij} (if $i = j$, $\delta_{ij} = 1$; otherwise, $\delta_{ij} = 0$). Any perturbation to E_z will shift the energy level accordingly. Therefore, the broken bond induced bond energy gain will shift positively the core level. Incorporating the BOLS notion into Eq.(2) yields the energy shift of the vth energy level of z-coordinationed atom from that of the isolated atom, for the monolayer skin and the core-shell configured nanocrystals:

$$\Delta E_v(z) = E_v(z) - E_v(0) = \Delta E_v(12)\left(1+\Delta_H\right)$$

where,

$$\Delta_H = \begin{cases} C_z^{-1} - 1 & \text{(Skin effect)} \\ \tau K^{-1}\sum_{i\le 3} C_z\left(C_z^{-1}-1\right) & \text{(Size effect)} \end{cases} \quad (3)$$

The solid skins and atomic clusters are thus unified. The shape factor τ = 3, 2, and 1 corresponds to a sphere dot, a cylindrical rod, and a thin plate, respectively. K represents the dimensional radius equaling to R/d_b, where R is the real size of the specimen and d_b is the bulk bond length of the corresponding material. The sum starts from the outermost atomic layer inward up to three because of the negligible bonder loss.

2.2 Skin- and size-resolved BE shift

An XPS profile consists of components corresponding to skins (S_i) and bulk (B) contributions with each component being characterized by an optimal value of z. The fraction of the specifically z-coordinated atoms

determines the intensities of the components. The $E_v(0)$ and the z-dependent $\Delta E_v(z)$ of the skin satisfy the criterion[9]:

$$\frac{E_v(z)-E_v(0)}{E_v(z')-E_v(0)}=\frac{C_z^{-1}}{C_{z'}^{-1}}\ (z'\neq z)\ \ or\ \ E_v(0)=\frac{C_{z'}E_v(z')-C_zE_v(z)}{C_{z'}-C_z}\quad (z'\neq z)$$

$$\Delta E_v(z)=E_v(z)-E_v(0)=\left[E_v(12)-E_v(0)\right]\times C_z^{-1} \tag{4}$$

We can determine the $E_v(0)$ and the corresponding bulk shift $\Delta E_v(z=12)$ by decomposing XPS spectra using constraint of Eq.(4). Besides, we can also predict the coordination-resolved atomic cohesive energy ($E_{\mathrm{Coh}} = E_{\mathrm{Coh}}(z)/ E_{\mathrm{Coh}}(12) = z_{ib}C_z^1$) and the local binding energy density ($E_{\mathrm{Den}} = [E_{\mathrm{Den}}(z)/ d_i^3] / [E_{\mathrm{Den}}(12)/ d_b^3] = C_z^4$) at the specific atomic site. The ratio $z_{ib} = z /12$ is the relatively atomic coordination number with $z_b = 12$ being the bulk value for the face-centered cubic (fcc) structure. These quantities are of fundamental importance to the understanding of the skin and the processes of bond and electron relation relaxation at the kink, edge and defect skin. These elemental quantities determine the performance of the undercoordinated system. For example, the energy density determines the mechanical strength, the atomic cohesive energy determines thermal stability and the quantum entrapment or electron polarization determines the chemical reactivity[9].

In fact, shorter and stronger bonds at the skin dominate the size effect on the core level shift. Using the sum rule of the core−shell structure and taking the surface-to-volume ratio[36, 37] into effect, the radius K dependent vth atomic energy level $E_v(K)$ and its bulk shift $\Delta E_v(12)$ of nanocrystal can be deduced,

$$E_v(K)=E_v(12)+\Delta E_v(12)\Delta_H=E_v(12)+\tau K^{-1}\Delta E_v(12)\sum_{i\le 3}C_z\left(C_z^{-1}-1\right)$$

$$\Delta E_v(12)=E_v(12)-E_v(0) \tag{5}$$

If a cluster approximates a sphere, the number of atoms represented as $N = 4\pi K^3/3$, and its radius K follows $K^{-1} = (3N/4\pi)^{-1/3} \approx 1.61N^{-1/3}$. Then, we can obtain $E_v(N) = A + 1.61BN^{-1/3}$. So we can correlate the shape τ, size N,

and the relaxation of the core level BE using Eq.(5):

$$E_v(N) = E_v(12) + 1.61\tau\Delta E_v(12)\sum_{i\le 3} C_z\left(C_z^{-1} - 1\right)N^{-1/3} \tag{6}$$

Measurements revealed the linear relationship $E_v(K) = A + BK^{-1}$ for the size effect on core level shift[9], where A and B are corresponding to y-axis intercept and slope in the linear relationship, respectively. In comparison to measurements, one can derive:

$$\begin{cases} A = E_v(12) \\ B = \tau\Delta E_v(12)\sum_{i\le 3} C_z\left(C_z^{-1} - 1\right) \end{cases}$$

and,

$$\tau = B\Big/\Delta E_v(12)\sum_{i\le 3} C_z\left(C_z^{-1} - 1\right) \tag{7}$$

2.3 Zone-selective photoelectron spectrometric (ZPS)

An invention of the ZPS[38] has enabled distillation of atomistic, local, and quantitative information on the electronic bonding energy at irregularly coordinated atomic sites such as defect, edges, skins, impurities, and interfaces. The ZPS proceeds by subtracting the XPS reference spectrum from XPS profiles[39] collected from the conditioned skins. The referential XPS spectrum is collected from the ideally perfect skin of the same substance. Before subtraction, we need to correct the spectral background[40, 41] and normalize the specific peak before decomposing into components. Then ZPS distills directly the skin or conditioned component as emerging peaks and the bulk component as a valley. Meanwhile, according to constrains on the component energy separation, Eq.(4), each XPS spectrum is decomposed into the skin (S_i) components and the bulk component (B) with optimization of the respective z value by fitting to the entire spectral peak.

2.4 DFT calculations

Calculation of the bond contraction and BE shift for the optimal Rb and Cs clusters of a variety structure[42, 43] (as shown in Figure 1) was performed using the DFT method. The DFT method[44, 45] used the Vienna Abolition simulation package that based on the plane-wave pseudopotential. In our calculation, the exchange-correlation potential used the generalized gradient approximation (GGA)[46] and Perdew, Burke and Ernzerhof (PBE)[47]. The energy cutoff was 400 eV. The Brillouin zone of the cell was performed within the Monkhorst–Pack grids using 1×1×1 *k* points. The cell size is 27×27×27 Å. All atoms were fully relaxed by using the conjugate gradient method and the optimal atomic positions are determined until converge the total energy within 0.01 meV.

Calculation was also focused on the charge transfer of undercoordinated atoms, which was performed using the $DMol_3$ code with a double numerical plus polarization (DNP) basis set[48]. In the process, we used Mulliken population analysis[49] with the spin-polarized code for Rb and Cs edge states, and the self-consistency threshold of the total energy was maintained at 10^{-6} au.

3. Results and discussion

3.1 Skin Rb 4*p* and Cs 5*p* energy shift

G. K. Wertheim et al. have measured Rb 4*p* photoemission spectrum[50] of as-deposited Rb surfaces at 80 K with a range of photon energies from 22 up to 65 eV, and Cs 5*p* photoemission spectrum[51] of a Cs surface at 100 K with photon energy of 21.2 eV. The XPS spectra of the Rb(110) 4*p* level under $h\nu$ = 65 eV beam excitation and the Cs(110) 5*p* level under $h\nu$ = 21.2 eV incident beam energy, shown in Figure 2a and 2b suggest that these spectra contain each three components from higher to lower BE, whose peak energies are constrained by Eq.(4). Differentiating the Rb(110) skin[50] 4*p* spectra collected using $h\nu$ = 45 eV and $h\nu$ = 65 eV beam energies gives immediately the bulk component as a valley centered at B = 14.940 eV and the monolayer skin at S_1 = 15.127 eV. The spectrum collected at 45 eV beam energy collects more skin information than the higher energy beam[9]. Table 1 features the derived information.

In the spectrometric analysis, one needs to determine the $E_v(0)$ firstly, which is proceeded as follows. If l (> 2)

sublayer components are involved in a set of XPS spectra collected from skins of a specific substance of different registries, the $E_v(0)$ and the $\Delta E_v(12)$ take the mean value of $N = C(l,2) = l!/[(l\text{-}2)!2!]$ possible combinations with the standard deviation σ, [9]

$$\begin{cases} E_v(z) &= < E_v(0) > \pm\sigma + \Delta E_v(12)\left(1+\Delta_H\right) \\ < E_v(0) > &= \sum_N E_{vl}(0)/N \\ \sigma &= \sqrt{\sum_{C(l,2)}\left[E_{vl}(0) - < E_v(0) >\right]^2 \Big/ \left[N(N+1)\right]} \end{cases} \tag{8}$$

The (110) skin has a total of $l = 3$ components. There will be $N = C(3,2) = 3$ different $E_v(0)$ values for averaging. The $E_v(0)$ and $\Delta E_v(12)$ are intrinsic for a specific material and they are independent of the crystal structure, experimental conditions, and other factors[52]. One can get the $\Delta E_v(12)$ by decomposing the XPS spectrum, for Rb $\Delta E_{4p}(12) = 1.286$ eV and for Cs $\Delta E_{5p}(12) = 1.546$ eV. Calculations derived the z-resolved Rb 4p and Cs 5p level shift:

$$\begin{aligned} E_{4p}(z) &= 13.654 \pm 0.003 + 1.286 C_z^{-1} \quad (\text{Rb skins}) \\ E_{5p}(z) &= 10.284 \pm 0.005 + 1.546 C_z^{-1} \quad (\text{Cs skins}) \end{aligned} \tag{9}$$

The z-resolved Rb 4p and Cs 5p energy shift enables quantification of the atomic-site resolved bond strain ε_z, relative bond energy δE_z, relative atomic cohesive energy δE_{Coh}, and relative energy density δE_{Den} in the outermost three atomic layers as a function of the z, as shown in Table 1. Results show that the atomic undercoordination enhances the local strain and energy density but depresses the atomic cohesive energy, as shown in Figure 3 and Table 1. The energy density determines the elasticity and the cohesive energy determines the thermal stability of the solid skin.

3.2 Cluster Rb and Cs energy shift

Figure 4 shows the shell-resolved Rb 4p and Cs 5p local density of states (LDOS) for the atomic clusters,

which resolves the atomic site resolved bond length, bond energy, energy density, atomic cohesive energy, and the effective atomic coordination numbers[52]. Combining Eqs. (1)and (3) yields[9],

$$z = 12 \Big/ \left\{ 8\ln\left(\frac{2\Delta E_v(z) - \Delta E_v(12)}{\Delta E_v(12)} \right) + 1 \right\} \tag{10}$$

With the known $\Delta E_{4p}(12)$ for Rb, $\Delta E_{5p}(12)$ for Cs, and $\Delta E_v(z) = E_v(z) - E_v(12)$, we are able to calculate the atomic CN of $C_1$28, O_h44, C_{3v}46 and O_h55 clusters using Eq.(10). Figure 5a exhibits the atomic CN-resolved core level shift of different structures. For example, the CNs of the fourth and fifth atoms in the Cs_{28}, the third atom in the Cs_{44}, the first atom in the Cs_{46} and the second atom in the Cs_{55} are the same CN values, it is 3.470. Therefore, the local BE shifts are the same if atoms have the same CN value, as compared in Table 2. We also find that the smaller the effective CN is, the larger the BE shift[9]. Besides, we calculated the cluster for $N = 28$ with GGA and PBE functions, and found that calculations using these two functions result in the same size trend albeit the absolute values, as shown in Figure 5b. Therefore, it is more meaningful to focus on the nature and trend of the atomic CN induced relaxation than on the algorithms employed.

3.3 Bond strain, energy entrapment, and electron polarization

The DFT derived bond lengths in Rb and Cs clusters, shown in Table 3 suggest that atomic undercoordination shortens the local bond, as we expected. The results are consistent with the reported bond contractions of Na, K, Fe, Cu, Ni and Pd atomic chains[53]. We also estimated the charge transfer (Mulliken population analysis[49]) of Rb and Cs nanocrystals(shown in Figure 1b) and found that the undercoordinated skin atom 1 gain charge from the inner atom 2, see Table 3. Such electron transition from the inner to the outermost layer agrees that demonstrated by Mo nanoclusters[54]. such electron polarization responsible for dilute magnetism and n-type catalytic behavior[9].

Figure 6 unifies the DFT computation and BOLS prediction on the cluster size dependence of the BE quantum entrapment of Rb and Cs clusters. Results in Figure 6a and 6b show that cluster size N reduction shifts the peak toward deeper binding energies, as summarized in Table 3. For example, the Rb 4*p* level shifts positively

from 0.368 to 0.604 eV associated with atomic CN reduction from 2.643 to 1.925 when the N is decreased from 55 to 13, which is consistent with the reported size and shape energy shift trend for Mo[54]. Therefore, the cluster size reduction shortens and stiffens its bonds. The spontaneous bond contraction leads to local densification, quantum entrapment of binding energy, and charge polarization, which leads to globally positive core level shift[25, 52].

3.4 *N*- resolved $E_v(N)$

According to the BOLS convention[9], energy levels for atoms having the same CN will shift the same amount. We can therefore derive the N-dependent core level shift. Picking first and second atomic layers of the nanoclusters as the references of known CN, for instance, the first and fifth atoms of Rb_{28} with respective z_1 = 2.197 and z_2 = 4.320, we can obtain immediately C_1 = 0.7281, C_2 = 0.8893, and the sum $\Delta'_H = \sum_{i\le 3} C_{z_i}(C_{z_i}^{-1}-1)$ = 0.3826. Without any assumptions, we can use the known $\Delta E_{4p}(12)$ derived from the XPS and Eq.(6) to obtain the N-dependent BE shift[54]:

$$\begin{cases} E_{4p}(N) = E_{4p}^{\text{Fermi}}(12) + 0.792\tau N^{-1/3}(\text{eV}) & (\text{Experiment}) \\ E'_{4p}(N) = E'_{4p}(12) + 0.792\tau N^{-1/3}(\text{eV}) & (\text{Calculation}) \end{cases}$$

and the work function Φ,

$$\begin{cases} \Phi_1 = E_{4p}^{\text{Fermi}}(12) - E'_{4p}(12)\ (\text{eV}) \\ \Phi_2 = E_{4p}^{\text{vacuum}}(12) - E_{4p}^{\text{Fermi}}(12)\ (\text{eV}) \\ \Phi = \Phi_1 + \Phi_2 = E_{4p}^{\text{vacuum}}(12) - E'_{4p}(12)\ (\text{eV}) \end{cases} \tag{11}$$

The vacuum (E_{4p}^{vacuum}) and fermi (E_{4p}^{Fermi}) levels represent binding energies for 4p electrons in the atomic and solid states of Rb. The work function Φ_2 = 2.18 eV for Rb cluster[55] and E_{4p}^{Fermi} = 14.940 eV. Figure 6c plots the $N^{-1/3}$ linear dependence of the $E_{4p}(N)$ for Rb nanoclusters. The linear relationship gives the y-intercept of 12.620 eV and the slope of 1.397. Hence, we can determine the shape factor τ = 1.763 with Eq.(7) and Φ_1 = 2.32 eV of Rb clusters. Then we can obtain Φ = 4.50 eV for Rb, which is the difference in the DFT calculations ground state $E_{4p}^{\text{vacuum}}(12)$ and the experiments excited state $E'_{4p}(12)$ of bulk value. Similarly, we

choose the first and fifth atoms of Cs_{28} cluster as the references of known CN for the first and second atomic layers of Cs nanoclusters. After that, we have Φ_2 = 2.14 eV [55], E_{5p}^{Fermi} = 11.830 eV, the *y*-intercept is 10.280 eV, the slope is 1.493, τ = 1.790, and Φ = 3.69 eV for Cs cluster. So *N*-resolved $E_{4p}(N)$ of Rb and $E_{5p}(N)$ of Cs can be described:

$$\begin{cases} E_{4p}(N) = 14.940 + 1.397N^{-1/3}(\text{eV}) & (\text{Rb Experiment}) \\ E'_{4p}(N) = 12.620 + 1.397N^{-1/3}(\text{eV}) & (\text{Rb Calculation}) \end{cases}$$

$$\begin{cases} E_{5p}(N) = 11.830 + 1.493N^{-1/3}(\text{eV}) & (\text{Cs Experiment}) \\ E'_{5p}(N) = 10.280 + 1.493N^{-1/3}(\text{eV}) & (\text{Cs Calculation}) \end{cases} \quad (12)$$

Figure 6c and 6d show the consistence in BOLS prediction, DFT calculation, and XPS measurement about the core-level BE. Among them, the core-level 4*p* photoelectron spectra of free and neutral Rb clusters for four different sizes[56] (*N* = 40, 90, 110, 170) were measured using constant photon energy of 40 eV.

Combining Eqs.(6) and (10) with the known ΔE_v(12), we can formulate the effective CN as a function of cluster size *N*:

$$z = \begin{cases} 12 \Big/ \left\{ 8\ln\left(2.173N^{-1/3} + 1\right) + 1 \right\} & (\text{Rb}_{\text{N}} \text{ clusters}) \\ 12 \Big/ \left\{ 8\ln\left(1.931N^{-1/3} + 1\right) + 1 \right\} & (\text{Cs}_{\text{N}} \text{ clusters}) \end{cases} \quad (13)$$

Then, we can obtain the corresponding CN using Eq.(13) and the bond contraction coefficient:

$$C_z = \begin{cases} 2 \Big/ \left(2.173N^{-1/3} + 2\right) & (\text{Rb}_{\text{N}} \text{ clusters}) \\ 2 \Big/ \left(1.931N^{-1/3} + 2\right) & (\text{Cs}_{\text{N}} \text{ clusters}) \end{cases} \quad (14)$$

We can also predict the *N*-resolved local strain, relative atomic cohesive energy and relative energy density. Figure 7 and Table 3 show the *N* dependence of the atomic CN, strain, and energies of Rb and Cs clusters. Cluster size *N* reduction enhances the energy shift and energy density but reduces the CN, local strain, and cohesive energy[4, 57, 58], associated with polarization. Such a consistency between DFT calculations and BOLS predictions evidences that local bond contraction and quantum entrapment lead to a densification of the charge and energy surrounding the undercoordinated atomic sites, which result in a positive BE shift for Rb and Cs skins and nanocrystals.

4. Conclusion

The combination of DFT calculations and XPS measurements has verified our BOLS prediction, and clarified that the shorter and stronger bonds between undercoordinated atoms are responsible for the size and skin effect on the energy entrapment, densification and electron polarization of Rb and Cs skins and nanocrystals. Observations will be helpful for understanding the unusual behavior of solid skins and nanocrystals in practical applications and will provide powerful means for designing and fabricating nanostructures with desired properties.

Acknowledgement

Financial supports from the NSF (Grants Nos. 11502223 and 11402086) are gratefully acknowledged.

Table and Figure captions:

Table 1 BOLS-ZPS derived effective CN (z), bond strain ε_z, relative bond energy δE_z, relative atomic cohesive energy δE_{Coh}, and relative energy density δE_{Den} in various registries of Rb and Cs skins.[a]

	i	z	Rb(110)		Cs(110)		z_{ib} (%)	$-\varepsilon_z$ (%)	δE_z (%)	$-\delta E_{\mathrm{Coh}}$ (%)	δE_{Den} (%)
			E_{4p} (i)	ΔE_{4p} (i)	E_{5p} (i)	ΔE_{5p} (i)					
Atom	-	0	13.654	-	10.284	-	0	-	-	-	-
Bulk	B	12.00	14.940	1.286	11.830	1.546	100	0	0	0	0
(110)	S2	5.83	15.029	1.375	11.940	1.656	48.583	6.605	7.072	47.981	31.433
	S1	3.95	15.127	1.473	12.053	1.769	32.917	12.669	14.507	62.308	71.919

[a] Sublayers S_i of the same registry share their common z value regardless of the chemical composition. With the optimal z and known m (m = 1)[34] value, one can readily derive the bond strain $\varepsilon_z = C_z - 1$, relative increases of bond energy $\delta E_z = C_z^{-1} - 1$, binding energy density $\delta E_{\mathrm{Den}} = C_z^{-4} - 1$, and the atomic cohesive energy $\delta E_{\mathrm{Coh}} = zC_z^{-1}/12 - 1$ in the respective sublayer accordingly.

Table 2 The average effective CN, core level shift ΔE_z, bond strain ε_z, relative bond energy δE_z and relative energy density δE_{Den} in various registries of Rb and Cs clusters with GGA functions.

	Atom position	$E_{4p}(i)$	z	ΔE_z	z_{ib} (%)	$-\varepsilon_z$ (%)	δE_z (%)	δE_{Den} (%)		$E_{5p}(i)$	z	ΔE_z	z_{ib} (%)	$-\varepsilon_z$ (%)	δE_z (%)	δE_{Den} (%)
Rb_{28}	1	13.374	2.197	0.480	18.308	27.186	37.337	255.753	Cs_{28}	11.102	2.527	0.462	21.058	23.010	29.887	184.618
	2	13.267	2.575	0.373	21.458	22.485	29.008	176.990		10.972	3.110	0.332	25.917	17.678	21.474	117.740
	3	13.214	2.836	0.320	23.633	19.926	24.884	143.234		10.918	3.470	0.278	28.917	15.244	17.986	93.785
	4	13.214	2.836	0.320	23.633	19.926	24.884	143.234		10.918	3.470	0.278	28.917	15.244	17.986	93.785
	5	13.054	4.320	0.160	36	11.066	12.442	59.853		10.825	4.417	0.185	36.808	10.689	11.968	57.173
	6	12.894	12	0	100	0	0	0		10.640	12	0	100	0	0	0
Rb_{44}	1	13.368	1.949	0.582	16.242	31.160	45.264	345.275	Cs_{44}	11.089	2.048	0.646	17.067	29.470	41.785	304.126
	2	13.262	2.209	0.476	18.408	27.014	37.014	252.414		10.905	2.527	0.462	21.058	23.010	29.887	184.618
	3	12.998	3.659	0.212	30.492	14.152	16.485	84.109		10.721	3.470	0.278	28.917	15.244	17.986	93.785
	4	12.786	12	0	100	0	0	0		10.443	12	0	100	0	0	0
Rb_{46}	1	13.403	3.169	0.268	26.408	17.243	20.835	113.195	Cs_{46}	11.091	3.470	0.278	28.917	15.244	17.986	93.785
	2	13.349	3.638	0.214	30.317	14.268	16.642	85.107		10.998	4.417	0.185	36.808	10.689	11.968	57.173
	3	13.295	4.320	0.160	36	11.066	12.442	59.853		10.906	6.287	0.093	52.397	5.673	6.014	26.317
Rb_{55}	1	13.371	2.836	0.320	23.633	19.926	24.884	143.234	Cs_{55}	11.013	2.901	0.371	24.175	19.356	24.002	136.433
	2	13.211	4.320	0.160	36	11.066	12.442	59.853		10.920	3.470	0.278	28.917	15.244	17.986	93.785
	3	13.051	12	0	100	0	0	0		10.642	12	0	100	0	0	0

Table 3 The core level shift $\Delta E_v(i)$, bond length d_i, bond strain ε_z, relative atomic cohesive energy δE_{Coh} and relative energy density δE_{Den} in various registries of Rb and Cs nanocrystals.

	N	$E_v(i)$	z	$\Delta E_v(i)$	d_{12}(Å)	Charge [a] (atom 1/2)	z_{ib} (%)	$-\varepsilon_z$ (%)	$-\delta E_{\mathrm{Coh}}$ (%)	δE_{Den} (%)
Rb_N (DFT)	13	13.224	1.924	0.604	4.564	-0.028/0.339	16.036	31.604	76.554	356.964
	28	13.127	2.256	0.507	4.529	-0.048/0.007	18.804	26.352	74.468	239.897
	36	13.125	2.378	0.505	4.402	-0.003/0.108	19.820	24.758	73.658	212.008
	53	13.033	2.580	0.413	4.414	-0.032/0.065	21.497	22.435	72.285	176.278
	55	12.988	2.600	0.368	4.472	-0.037/0.089	21.665	22.221	72.145	173.248
	Bulk	12.620	12	0	4.936	--	100	0	0	0
Rb_N (Exp)	40	13.090[b]	2.355	0.470	--	--	19.625	25.052	73.815	216.933
(Φ=4.50eV)	90	12.980[b]	2.836	0.360	--	--	23.633	19.926	70.485	143.234
	110	12.960[b]	2.953	0.340	--	--	24.608	18.917	69.650	131.359
	170	12.910[b]	3.308	0.290	--	--	27.567	16.276	67.074	103.519
Cs_N (DFT)	13	10.804	2.070	0.524	4.903	-0.032/0.385	17.250	29.115	75.665	296.073
(Φ=3.69eV)	25	10.798	2.373	0.518	4.846	-0.021/0.016	19.775	24.826	73.694	213.130
	28	10.774	2.430	0.494	4.683	-0.045/0.060	20.250	24.129	73.310	201.782
	35	10.746	2.547	0.466	4.962	-0.021/0.096	21.225	22.789	72.510	181.375
	53	10.667	2.778	0.387	4.963	-0.005/0.044	23.150	20.455	70.897	149.777
	58	10.738	2.831	0.458	4.934	-0.006/0.008	23.592	19.970	70.521	143.779
	Bulk	10.280	12	0	5.317	--	100	0	0	0

[a] Negative sign means charge gain otherwise charge loss.

[b] Data for Rb_{40}, Rb_{90}, Rb_{110}, Rb_{170} is the experimental value[56] minus the value of $\Phi = E_v^{\mathrm{vacuum}}(12) - E_v'(12)$.

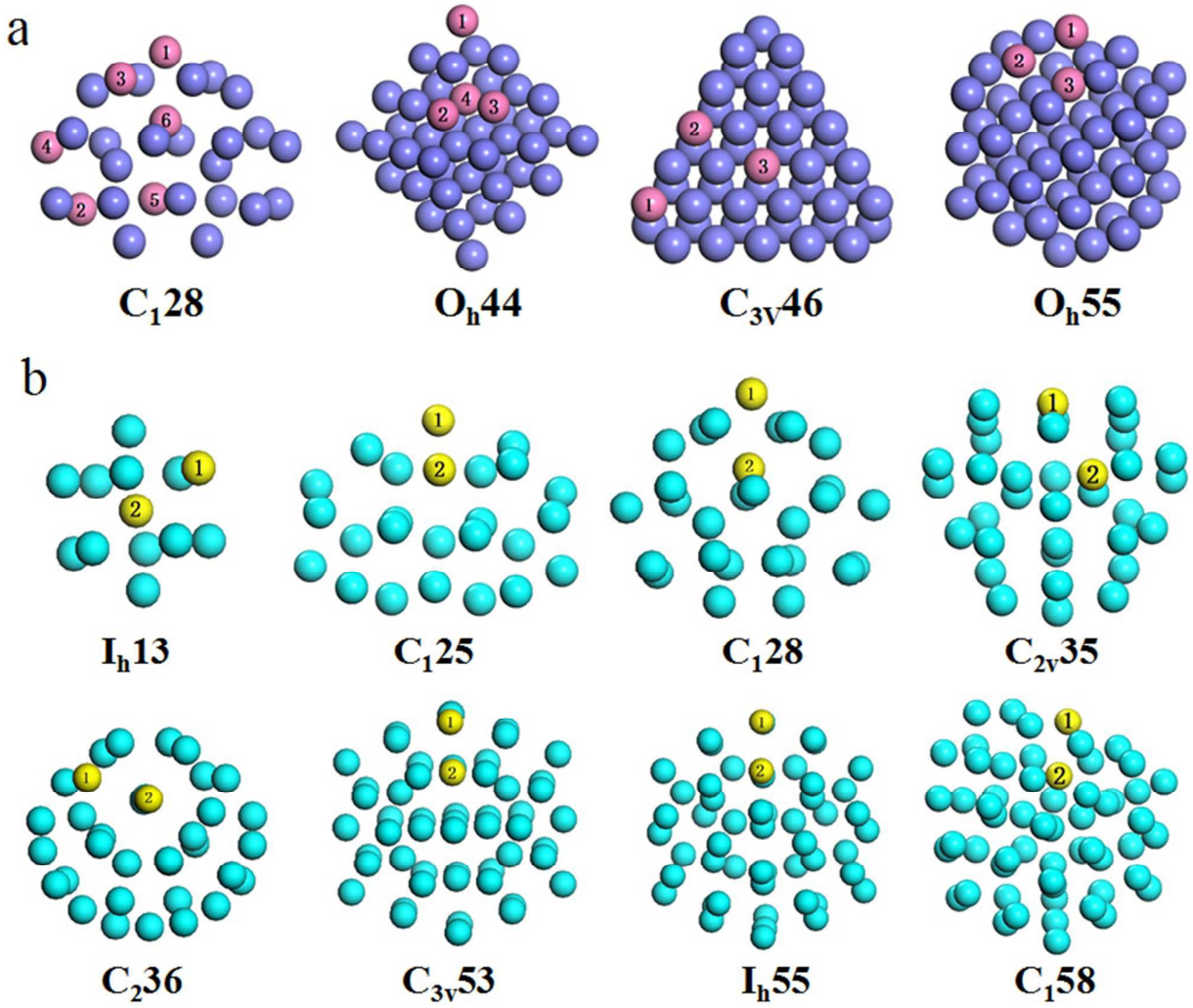

Figure 1 Geometric configurations of (a) $C_1$28, O_h44, C_{3v}46 and O_h55 for Rb and Cs clusters, (b) I_h13, $C_1$28, $C_2$36, C_{3v}53 and I_h55 for Rb clusters, and I_h13, $C_1$25, $C_1$28, C_{2v}35, C_{3v}53 and $C_1$58 for Cs clusters.

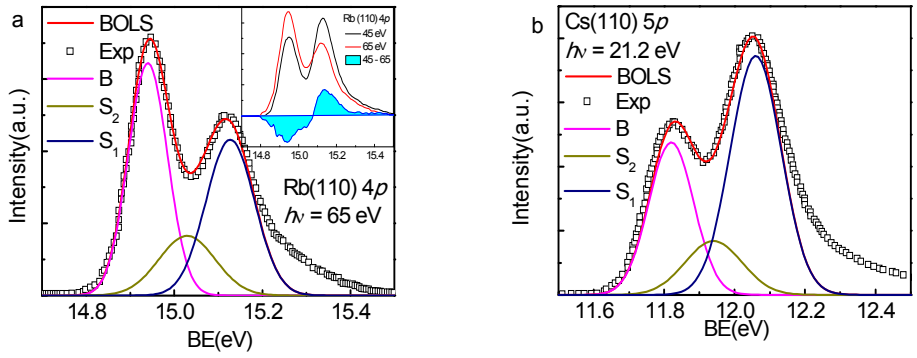

Figure 2 BOLS−TB decomposition of the XPS spectra for (a) Rb(110) 4*p* collected at 65 eV beam energy and (b) Cs(110) 5*p* collected at 21.2 eV beam energy with the bulk B, S_2, and S_1 components. Table 1 features the derived information. The inset (a) shows the ZPS (difference between spectra collected using 45 eV and 65 eV beam energies[9]) distills the bulk valley (B = 14.940 eV) and the monolayer skin component (S_1 = 15.127 eV).

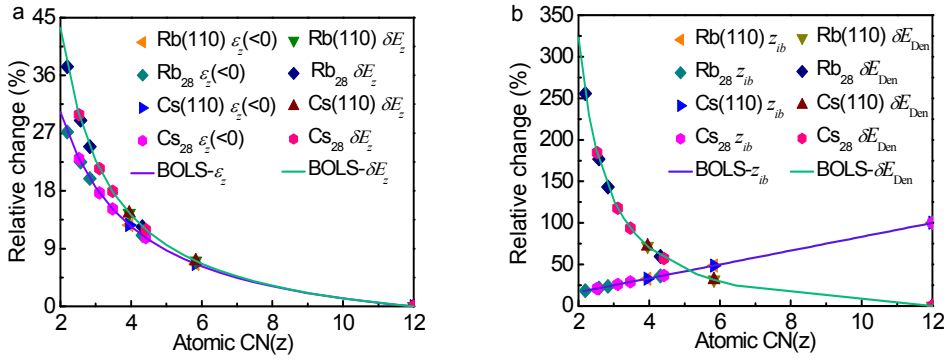

Figure 3 Atomic site resolved (a) bond strain ε_z, relative bond energy δE_z, (b) effective CN z_{ib} and relative energy density δE_{Den} for Rb and Cs skins and clusters.

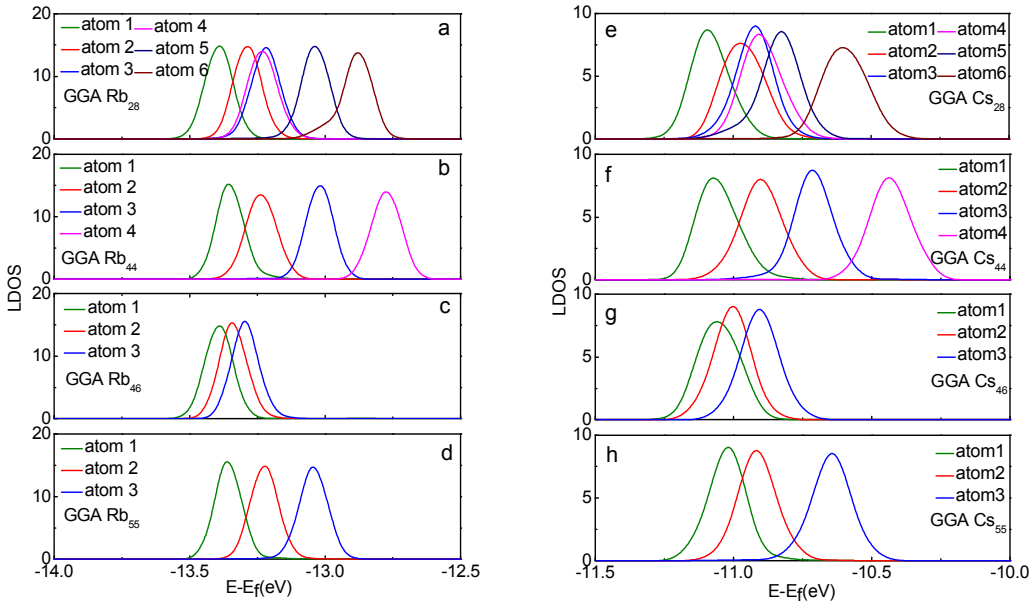

Figure 4 Shell-resolved LDOS for (a, e) $C_1$28, (b, f) O_h44, (c, g) C_{3v}46, and (d, h) O_h55 clusters of Rb and Cs clusters.

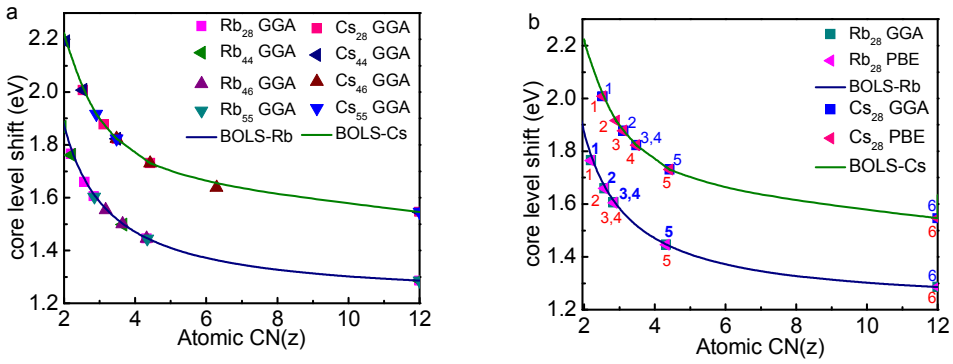

Figure 5 Atomic CN-resolved core level shift of Rb and Cs clusters derived using (a) GGA approach and (b) compared with PBE functions for $N = 28$ clusters.

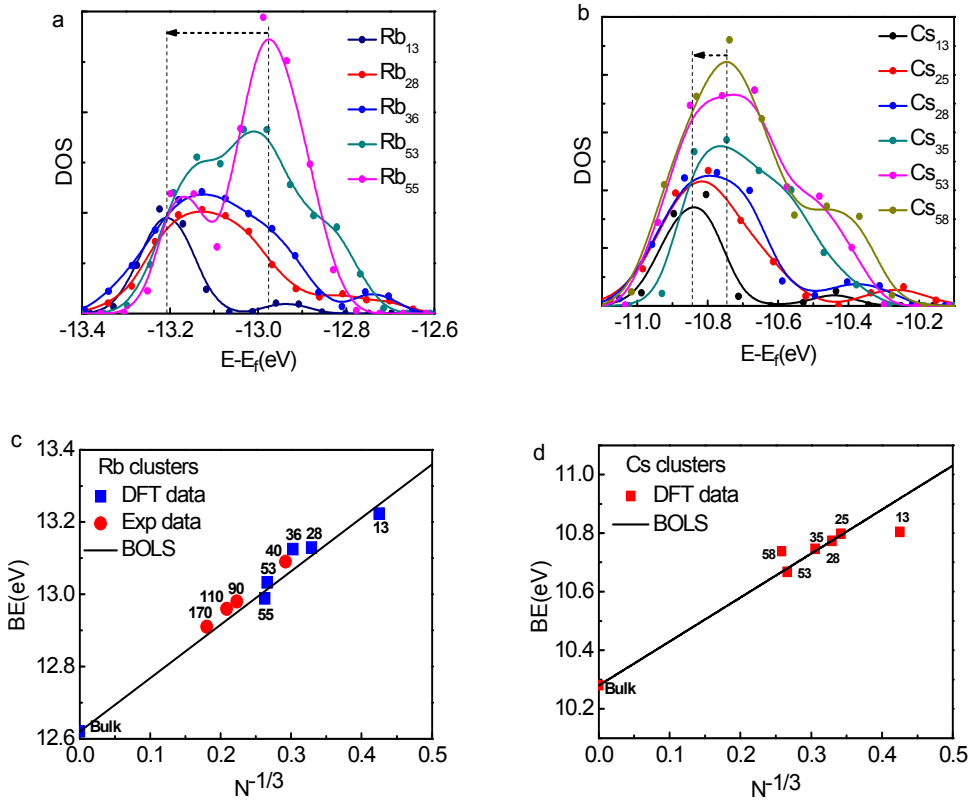

Figure 6 DFT derived (a, b) core level quantum entrapment of Rb_N and Cs_N clusters matches (c, d) the BOLS predictions. Data for Rb_{40}, Rb_{90}, Rb_{110} and Rb_{170} are measurements sourced from[56] minus the value of $\Phi = E_v^{\text{vacuum}}(12) - E_v'(12)$.

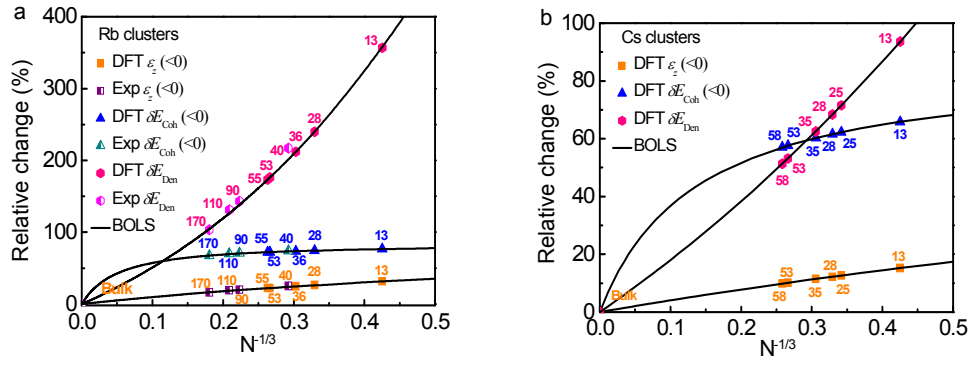

Figure 7 Consistency in the BOLS predicted, experimentally measured, and DFT derived N dependence of the bond strain ε_z, relative atomic cohesive energy δE_{Coh} and relative energy density δE_{Den} for (a) Rb and (b) Cs nanocrystals.

A table of contents entry：

Coordination environment resolves electron binding-energy shift of Rb and Cs clusters.

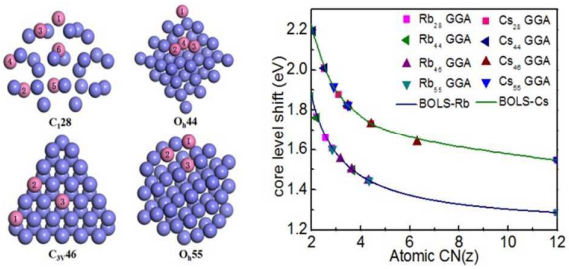

References:

1. L. Pauling, *J. Am. Chem. Soc.* 1947, **69**, 542-553.
2. C. Q. Sun, *Relaxation of the Chemical Bond*, Springer Singapore2014.
3. R. Ahlrichs and S. D. Elliott, *Phys. Chem. Chem. Phys.* 1999, **1**, 13-21.
4. C. C. Yang and S. Li, *Phys. Rev. B* 2007, **75**, 1654131-1654135.
5. B. Balamurugan, B. R. Mehta, D. K. Avasthi, Fouran Singh, Akhilesh K. Arora, M. Rajalakshmi, A. G. Raghavan, K. Tyagi and S. M. Shivaprasad, *J. Appl. Phys.* 2002, **92**, 3304-3310.
6. O. Kostko, B. Huber, M. Moseler and B. von Issendorff, *Phys. Rev. Lett.* 2007, **98**, 0434011-0434014.
7. X. Wang, R. Q. Zhang, S. T. Lee, T. A. Niehaus and T. Frauenheim, *Appl. Phys. Lett.* 2007, **90**, 1231161-1231163.
8. S. J. Xu, S. J. Chua, B. Liu, L. M. Gan, C. H. Chew and G. Q. Xu, *Appl. Phys. Lett.* 1998, **73**, 478-480.
9. X. Liu, X. Zhang, M. Bo, L. Li, H. Tian, Y. Nie, Y. Sun, S. Xu, Y. Wang, W. Zheng and C. Q. Sun, *Chem. Rev.* 2015, **115**, 6746-6810.
10. B. R. Cuenya, *Thin Solid Films* 2010, **518**, 3127-3150.
11. W. J. Harper and W. J. Choyke, *J. Appl. Phys.* 1956, **27**, 1358-1360.
12. S. Park, T. Kim, Y. M. Chung, S. H. Oh and I. Song, *Res. Chem. Intermed.* 2010, **36**, 639-646.
13. G. Berger, J. Schott and C. Guy, *Chem. Geol.* 1988, **71**, 297-312.
14. C. Bélavári, E. Andrási, Z. Molnár and D. Gawlik, *Microchim. Acta* 2004, **146**, 187-191.
15. J. W. Flocken and J. R. Hardy, *Phys. Rev.* 1969, **177**, 1054-1062.
16. M. Endo, Y. Nakane, K. Takahashi, N. Hoshino, T. Takeda, S. Noro, T. Nakamura and T. Akutagawa, *J. Phy. Chem. B* 2015, **119**, 1768-1777.
17. D. Rayane, A.R. Allouche, E. Benichou, R. Antoine, M. Aubert-Frecon, Ph. Dugourd, M. Broyer, C. Ristori, F. Chandezon, B.A. Huber and C. Guet, *Eur. Phys. J. D* 1999, **9**, 243–248.
18. G. K. Wertheim, D. N. E. Buchanan and J. E. Rowe, *Solid State Commun.* 1991, **77**, 903–905.
19. S. H. Bauer, Yi‐Xue Zhang and C. F. Wilcox, *J. Chem. Phys.* 1999, **111**, 8265-8266.
20. B. Radisavljevic and A. Kis, *Nat. Mater.* 2013, **12**, 815-820.
21. R. Ravindran, K. Gangopadhyay, S. Gangopadhyay, N. Mehta and N. Biswas, *Appl. Phys. Lett.* 2006, **89**, 2635111-2635113.

22. M. G. Mason, *Phys. Rev. B* 1983, **27**, 748-762.
23. H. Shu, D. Cao, P. Liang, X. Wang, X. Chen and W. Lu, *Phys. Chem. Chem. Phys.* 2014, **16**, 304-310.
24. M. T. Oakley, R. L. Johnston and D. J. Wales, *Phys. Chem. Chem. Phys.* 2013, **15**, 3965-3976.
25. C. Q. Sun, *Nano.* 2010, **2**, 1930-1961.
26. C. Q. Sun, *Solid State Chem.* 2007, **35**, 1-159.
27. W. H. Qi, M. P. Wang and G. Y. Xu, *Chem. Phys. Lett.* 2003, **372**, 632-634.
28. L. Brus, *J. Chem. Phys.* 1983, **79**, 5566-5571.
29. J. Mawhin, *Critical point theory and Hamiltonian systems*, Springer Science & Business Media2013.
30. C.-Y. Lin, H.-W. Shiu, L.-Y. Chang, C.-H. Chen, C.-S. Chang and F. S.-S. Chien, *J. Phys. Chem. C* 2014, **118**, 24898-24904.
31. C. Chen, Y. Shi, Y. Zhang, J. Zhu and Y. Yan, *Phys. Rev. Lett.* 2006, **96**, 0755051-0755054.
32. P. W. Anderson, *Phys. Rev.* 1958, **109**, 1492-1505.
33. W. J. Huang, R. Sun, J. Tao, L. D. Menard, R. G. Nuzzo and J. M. Zuo, *Nat. Mater.* 2008, **7**, 308-313.
34. M. X. Gu, C. Q. Sun, Z. Chen, T. C. Au Yeung, S. Li, C. M. Tan and V. Nosik, *Phys. Rev. B* 2007, **75**, 1254031-1254039.
35. M. A. Omar, *Elementary solid state physics : principles and applications*, Addison-Wesley1975.
36. P. Hui and P. F. Yuan, *Acs Nano* 2008, **2**, 2410-2414.
37. G. Félix, W. Nicolazzi, M. Mikolasek, G. Molnár and A. Bousseksou, *Phys. Chem. Chem. Phys.* 2014, **16**, 7358-7367.
38. C. Q. Sun, Y. Nie, J. Pan, X. Zhang, S. Z. Ma, Y. Wang and W. Zheng, *RSC Adv.* 2012, **2**, 2377-2383.
39. V. Lockett, R. Sedev, C. Bassell and J. Ralston, *Phys. Chem. Chem. Phys.* 2008, **10**, 1330-1335.
40. A. Tejeda, R. Cortés, J. Lobo-Checa, C. Didiot, B. Kierren, D. Malterre, E. G. Michel and A. Mascaraque, *Phys. Rev. Lett.* 2008, **100**, 802-809.
41. J. E. Castle and A. M. Salvi, *J. Vac. Sci. Technol. A* 2001, **19**, 1170-1175.
42. Jonathan P.K.Doye, David J.Wales and R. Stephen Berry, *J. Chem. Phys.* 1995, **103**, 4234-4249.
43. Jonathan P. K. Doye, *Comput. Mater. Sci.* 2006, **35**, 227-231.
44. J. Hafner, *J Comput. Chem.* 2008, **29**, 2044-2078.
45. G.Kresse and J. Furthmüller, *Phys. Rev. B* 1996, **54**, 169-186.
46. J. P. Perdew, K. Burke and M. Ernzerhof, *Phys. Rev. Lett.* 1996, **77**, 3865-3868.

47. M. Ernzerhof and G. E. Scuseria, *J. Chem. Phys.* 1999, **110**, 5029-5036.

48. B. Delley, *J. Chem. Phys.* 1990, **92**, 508-517.

49. M. D. Segall, R. Shah, C. J. Pickard and M. C. Payne, *Phys. Rev. B* 1996, **54**, 16317-16320.

50. G. K. Wertheim, D. M. Riffe, N. V. Smith and P. H. Citrin, *Phys. Rev. B* 1992, **46**, 1955-1959.

51. G. K. Wertheim and D. N. E. Buchanan, *Phys. Rev. B* 1991, **43**, 13815-13818.

52. C. Q. Sun, *Phys. Rev. B* 2004, **69**, 0451051-0451058.

53. B. Delley, *Phys. Rev. B* 2002, **66**, 1551251-1551259.

54. W. Zhou, M. Bo, Y. Wang, Y. Huang, C. Li and C. Q. Sun, *RSC Adv.* 2015, **5**, 29663-29668.

55. H. L. Skriver and N. M. Rosengaard, *Phys. Rev. B* 1992, **46**, 7157-7168.

56. M. H. Mikkelä, M. Tchaplyguine, K. Jänkälä, T. Andersson, C. Zhang, O. Björneholm and M. Huttula, *Eur. Phys. J. D* 2011, **64**, 347-352.

57. W. H. Qi, *Solid State Commun.* 2006, **137**, 536-539.

58. X. Li, *Nanotechnology* 2014, **25**, 1857021-1857027.